
This copy is for your personal, non-commercial use only.

If you wish to distribute this article to others, you can order high-quality copies for your colleagues, clients, or customers by [clicking here](#).

Permission to republish or repurpose articles or portions of articles can be obtained by following the guidelines [here](#).

The following resources related to this article are available online at www.sciencemag.org (this information is current as of August 28, 2014):

Updated information and services, including high-resolution figures, can be found in the online version of this article at:

<http://www.sciencemag.org/content/342/6156/337.full.html>

Supporting Online Material can be found at:

<http://www.sciencemag.org/content/suppl/2013/10/16/342.6156.337.DC1.html>

A list of selected additional articles on the Science Web sites **related to this article** can be found at:

<http://www.sciencemag.org/content/342/6156/337.full.html#related>

This article **cites 29 articles**, 4 of which can be accessed free:

<http://www.sciencemag.org/content/342/6156/337.full.html#ref-list-1>

This article has been **cited by** 2 articles hosted by HighWire Press; see:

<http://www.sciencemag.org/content/342/6156/337.full.html#related-urls>

This article appears in the following **subject collections**:

Materials Science

http://www.sciencemag.org/cgi/collection/mat_sci

they reproduce the observed larger scatter and possibly higher normalization in SMBH-galaxy scaling relations for the most massive SMBHs (*1, 2*). Other physical effects will also be built into the next generation of GWB models. For example, recent numerical simulations of massive galaxy mergers predict binary SMBHs with eccentricities ranging between 0.1 (*31*) and 0.9 (*32*). If binaries radiating gravitational waves at frequencies relevant to pulsar timing arrays are considerably eccentric or predominantly evolving under environmental interactions (*33*), the spectral shape of $\Omega_{\text{GW}}(f)$ may differ from current predictions (*34*).

References and Notes

- J. Kormendy, L. Ho, *Annu. Rev. Astron. Astrophys.* **51**, 511–653 (2013).
- N. J. McConnell, C.-P. Ma, *Astrophys. J.* **764**, 184 (2013).
- D. J. Croton *et al.*, *Mon. Not. R. Astron. Soc.* **365**, 11–28 (2006).
- Q. Guo *et al.*, *Mon. Not. R. Astron. Soc.* **413**, 101–131 (2011).
- M. C. Begelman, R. D. Blandford, M. J. Rees, *Nature* **287**, 307–309 (1980).
- M. Volonteri, F. Haardt, P. Madau, *Astrophys. J.* **582**, 559–573 (2003).
- B. S. Sathyaprakash, B. F. Schutz, *Living Rev. Relativ.* **12**, 2 (2009).
- A. Sesana, A. Vecchio, C. N. Colacino, *Mon. Not. R. Astron. Soc.* **390**, 192–209 (2008).
- V. Ravi *et al.*, *Astrophys. J.* **761**, 84 (2012).
- G. B. Hobbs *et al.*, *Mon. Not. R. Astron. Soc.* **394**, 1945–1955 (2009).
- R. S. Foster, D. C. Backer, *Astrophys. J.* **361**, 300–308 (1990).
- R. van Haasteren *et al.*, *Mon. Not. R. Astron. Soc.* **414**, 3117–3128 (2011).
- P. B. Demorest *et al.*, *Astrophys. J.* **762**, 94 (2013).
- R. N. Manchester *et al.*, *Publ. Astron. Soc. Aust.* **30**, e017 (2013).
- J. P. W. Verbiest *et al.*, *Mon. Not. R. Astron. Soc.* **400**, 951–968 (2009).
- V. M. Kaspi, J. H. Taylor, M. F. Ryba, *Astrophys. J.* **428**, 713–728 (1994).
- D. R. B. Yardley *et al.*, *Mon. Not. R. Astron. Soc.* **414**, 1777–1787 (2011).
- The data sets are described in supplementary text section S1.
- Additional description of the algorithm is found in supplementary text section S2.
- R. Edwards, G. B. Hobbs, R. N. Manchester, *Mon. Not. R. Astron. Soc.* **372**, 1549–1574 (2006).
- W. Coles, G. Hobbs, D. J. Champion, R. N. Manchester, J. P. W. Verbiest, *Mon. Not. R. Astron. Soc.* **418**, 561–570 (2011).
- Details of the data challenge and other tests can be found in supplementary text section S2 and table S2.
- The algorithm used for calculating f_{PTA} is described in supplementary text section S3.
- Corrections to previous models for the GWB are outlined in supplementary text section S4. The models for the GWB are described in additional detail in supplementary text sections S5 and S6. The probabilities used to compare these models to the PPTA limit are calculated in supplementary text section S7.
- S. T. McWilliams, J. P. Ostriker, F. Pretorius, <http://arxiv.org/abs/1211.5377> (2012).
- A. Sesana, *Mon. Not. R. Astron. Soc.* **433**, L1–L5 (2013).
- V. Springel *et al.*, *Nature* **435**, 629–636 (2005).
- M. Boylan-Kolchin, V. Springel, S. D. M. White, A. Jenkins, G. Lemson, *Mon. Not. R. Astron. Soc.* **398**, 1150–1164 (2009).
- A. Kulier, J. P. Ostriker, P. Natarajan, C. N. Lackner, R. Cen, <http://arxiv.org/abs/1307.3684> (2013).
- Z. Haiman, *Astrophys. Space Sci. Library* **396**, 293–341 (2013).
- F. M. Khan, K. Holley-Bockelmann, P. Berczik, A. Just, *Astrophys. J.* **773**, 100 (2013).
- F. M. Khan *et al.*, *Astrophys. J.* **749**, 147 (2012).
- C. Roedig, A. Sesana, *J. Phys. Conf. Ser.* **363**, 012035 (2012).
- M. Enoki, M. Nagashima, *Prog. Theor. Phys.* **117**, 241–256 (2007).

Acknowledgments: We thank all of the observers, engineers, and Parkes observatory staff members who have assisted with the observations reported in this paper. We thank N. McConnell for providing and confirming some dynamical SMBH and bulge mass measurements, S. Mutch for discussions on the Millennium-based model, and X.-J. Zhu for comments on the manuscript. The Parkes radio telescope is part of the Australia Telescope National Facility, which is funded by the Commonwealth of Australia for operation as a National Facility managed by CSIRO. The Millennium and Millennium-II Simulation databases used in this paper and the Web application providing online access to these databases were constructed as part of the activities of the German Astrophysical Virtual Observatory. The PPTA project was initiated with support from R.N.M.'s Australian Research Council (ARC) Federation Fellowship (no. FF0348478) and from the CSIRO under that fellowship program. The PPTA project has also received support from ARC Discovery Project grant no. DP0985272. V.R. is a recipient of a John Stocker Postgraduate Scholarship from the Science and Industry Endowment Fund, G.H. is the recipient of an ARC QEII Fellowship (no. DP0878388), and J.S.B.W. acknowledges an Australian Research Council Laureate Fellowship. Part of this research was carried out at the Jet Propulsion Laboratory, California Institute of Technology, under a contract with NASA. J.P.W.V. acknowledges the financial support by the European Research Council (ERC) for the ERC Starting Grant Beacon under contract no. 279202. The authors declare no conflicts of interest. Data used in this analysis can be accessed via the Australia National Data Service (www.and.s.org.au).

Supplementary Materials

www.sciencemag.org/content/342/6156/334/suppl/DC1
Supplementary Text
Fig. S1
Tables S1 and S2
References (35–51)

19 March 2013; accepted 6 September 2013
10.1126/science.1238012

Strain-Induced Ultrahard and Ultrastable Nanolaminated Structure in Nickel

X. C. Liu,^{1*} H. W. Zhang,^{1*} K. Lu^{1,2†}

Heavy plastic deformation may refine grains of metals and make them very strong. But the strain-induced refinement saturates at large strains, forming three-dimensional ultrafine-grained (3D UFG) structures with random orientations. Further refinement of this microstructure is limited because of the enhanced mobility of grain boundaries. Very-high-rate shear deformation with high strain gradients was applied in the top surface layer of bulk nickel, where a 2D nanometer-scale laminated structure was induced. The strongly textured nanolaminated structure (average lamellar thickness of 20 nanometers) with low-angle boundaries among the lamellae is ultrahard and ultrastable: It exhibits a hardness of 6.4 gigapascal—which is higher than any reported hardness of the UFG nickel—and a coarsening temperature of 40 kelvin above that in UFG nickel.

Metals can be strengthened by introducing more grain boundaries (GBs) via grain refinement (*1, 2*) or alternatively by generating more dislocations (*3*). Remarkable hardening in metals and alloys induced through heavy plastic deformation originates from both mechanisms: Grains are refined to the sub-micrometer or nanometer scales, and stored

dislocation density is pumped up by orders of magnitude. However, as the strains exceed values between 5 and 30, saturation in grain refinement leads to steady-state three-dimensional (3D) ultrafine-grained (UFG, sub-micrometer-sized) structure with random orientations (*4–6*). Further increases in strain, however, can lead to grain coarsening and dislocation annihilation (*7, 8*). As

grain size drops into the submicro- or nanoscale, GB migration becomes so pronounced that grains coarsen even at ambient temperature (*9*). Because the dislocation multiplication from straining is balanced by the dislocation annihilation due to GB migration, strain-induced structural evolution ceases, and dislocation density reaches its limit, which in heavily deformed metals is typically $\sim 10^{15} \text{ m}^{-2}$.

Among various processing parameters of plastic deformation, strain rate, deformation temperature, and strain gradient seem most relevant to dislocation multiplication and, hence, to structure refinement or reduction of boundary spacing, which governs strength and other mechanical properties of materials. Deformation at high strain rates or at low temperatures may suppress dislocation annihilation kinetics and facilitate forming more GBs or dislocation boundaries. For instance, when nickel (Ni) is compressed at a rate

¹Shenyang National Laboratory for Materials Science, Institute of Metal Research, Chinese Academy of Sciences, Shenyang 110016, China. ²Herbert Gleiter Institute of Nanoscience, Nanjing University of Science and Technology, Nanjing 210094, China.

*These authors contributed equally to this work.

†Corresponding author. E-mail: lu@imr.ac.cn

of 10^2 and 10^3 s^{-1} to a strain of 2.9, a smaller boundary spacing with a higher dislocation density is formed relative to that under low-rate (10^{-2} s^{-1}) deformation, such as cold rolling and torsion, at comparable strains (10, 11). The fraction of low-angle boundaries becomes larger at higher strain rates (11, 12). Lowering deformation temperature may elevate stored dislocation density and reduce grain sizes in deformed copper (Cu) (12, 13). Strain gradient in plastic deformation is proportional to the density of stored geometrically necessary dislocations (14). A very high density of dislocations (1.8×10^{16} to $3.6 \times 10^{16} \text{ m}^{-2}$, which is one order of magnitude higher than the dislocation density limit in deformed Cu) is observed in thin shear bands in the nanotwinned structure in Cu, owing to the very high strain gradients (12).

In this work, a very-high-rate shear deformation with high strain gradients was applied in the top surface layer of a pure bulk Ni sample, where nanometer-thick laminated (NL) structures were induced. A pure Ni rod [purity of 99.88 weight percent (wt %)] of 10 mm in diameter was subjected to surface mechanical grinding treatment (SMGT) (Fig. 1A) at ambient temperature (15, 16), in which the rod surface layer is plastically sheared with gradient distributions of applied strain rates and strains. In the top surface layer of $\sim 80 \mu\text{m}$ thick, the estimated strain rate varies from 10^3 to 10^4 s^{-1} (topmost surface) to 10^2 to 10^3 s^{-1} ($80 \mu\text{m}$ deep from the treated surface), with corresponding accumulative equivalent strains of 30 to ~ 15 . Strain gradients in the top $80 \mu\text{m}$ vary from 0.4 to $0.1 \mu\text{m}^{-1}$, which is 10 times greater than that in the high-pressure torsion process (17). After the treatment, a depth-dependent gradient microstructure was formed (Fig. 1B): a nanostructured layer in the top surface of $\sim 80 \mu\text{m}$ thick with characteristic sizes below 100 nm , an UFG layer in a depth span of 80 to $\sim 140 \mu\text{m}$, and a deformation layer at $140 \mu\text{m}$ $\sim 1 \text{ mm}$ deep with various strain-induced defects, including dislocations and subboundaries. Deeper than 1 mm is deformation-free substrate.

The UFG layer is characterized by roughly equiaxed 3D grains (with an aspect ratio of <2), with an average size of $\sim 230 \text{ nm}$ and random orientations (Fig. 1, C and D). A large fraction of high-angle GBs ($>80\%$) was noticed from misorientation distribution measured by means of electron back-scattering diffraction (EBSD) and convergent beam electron diffraction (CBED) [in a transmission electron microscope (TEM)] (15). These are the typical characteristics of the steady-state UFG structures of Ni processed via heavy plastic deformation (4, 5, 18). The observed grain sizes and misorientation distribution agree quantitatively with those in the high-pressure torsion Ni samples with a strain of ~ 10 , which is comparable with the estimated accumulative strains in this section (~ 6 to ~ 14).

The topmost few micrometers of thickness are characterized by randomly oriented equiaxed nanograins with an average size of $\sim 11 \text{ nm}$. Deeper than

$10 \mu\text{m}$ are elongated nanosized grains (parallel to the sample surface), with an average transversal size of $18 \pm 5 \text{ nm}$ in cross-sectional TEM observations. With increasing depth from 10 to $50 \mu\text{m}$, no obvious change is seen for transversal sizes of the nanograins, but their aspect ratios increase markedly from a few to greater than 100. Most grains are several micrometers in length, whereas some are broken into sub-micrometer-long segments (Fig. 1, E and F). Similar morphologies were seen in the longitudinal-section TEM images, but with smaller aspect ratios (ranging from a few to ~ 15) (Fig. 1E) than the cross-sectional. Clearly, the subsurface layer in a depth span of 10 to $\sim 50 \mu\text{m}$ consists of 2D laminated grains, a kind of layer-shaped nanostructures (19). Rather uniform thickness is seen across the depth span of 10 to $\sim 50 \mu\text{m}$, ranging from 5 to 50 nm , averaging $20 \pm 7 \text{ nm}$ (Fig. 1E). Such NL structures are distinct from the steady-state UFG structures (Fig. 1C) from heavy plastic deformation.

In a depth span of 50 to $\sim 80 \mu\text{m}$ is a transition layer from the NL structures to the 3D UFG or nanograined (NG) structures, characterized by alternative layers consisting of slightly elongated nanograins (with an average transversal size of 70 nm) and NL structures. Thicknesses of both layers are roughly comparable.

The elongated diffraction spots in the selected area electron diffraction pattern (SAED) indicate a strong texture in the NL structures (Fig. 1E).

High-resolution TEM (HRTEM) observations were performed in order to identify the structure characteristics of boundaries between adjacent lamellae. Shown in Fig. 2A is a typical HRTEM observation of four lamellae (I to IV) along the $\langle 110 \rangle$ zone axis. From the fast Fourier transformation (FFT) (Fig. 2A, inset), one can see a small misorientation of $\sim 7^\circ$ along the $\langle 110 \rangle$ zone axis existing among these lamellae. HRTEM images showed that one of the closely packed $\{111\}$ planes of II (Fig. 2C) is inclined by 7° to that of III (Fig. 2D), which is in accordance with the splitting of (111) spots by an angle of 7° in the FFT. A zoom-in observation of the boundary (Fig. 2B) showed an inclination by 3° between the $\{111\}$ planes in II and III, implying an orientation gradient existing within the nanolamellae. Plenty of HRTEM images showed most boundaries in the NL structures exhibit similar misorientations along a certain axis, ranging from 1° to 8° .

Texture of the NL structures was determined with EBSD in a sample partially recovered at 540°C for 1 hour in order to improve the index rate while retaining the deformation texture. The $\{111\}$ pole figure (Fig. 2E) and orientation distribution function maps (fig. S2) showed that the texture components are major $\{100\}\langle 011 \rangle$ and minor $\{111\}\langle 112 \rangle$ and $\{111\}\langle 110 \rangle$ —typical torsion textures (pure shear) in FCC metals (20). The presence of the strong shear textures (with a

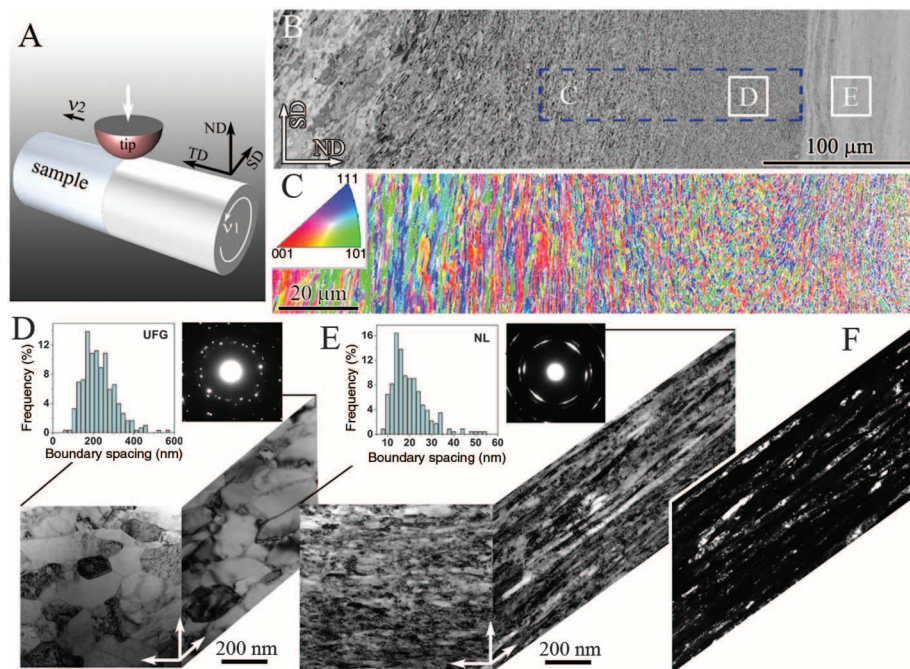


Fig. 1. Processing and microstructure overview of the Ni sample. (A) A schematic illustration of the SMGT setup. (B) A cross-sectional scanning electron microscope image of the SMGT Ni sample. The treated surface is outlined by a yellow dashed line. (C) An EBSD image of the region outlined by dashed blue line in B. (D and E) Typical bright-field cross-sectional (SD-ND) and longitude-sectional (TD-ND) TEM images of the UFG structures ($110 \mu\text{m}$ deep from the surface) and NL structures (40 to $50 \mu\text{m}$ deep from the surface) [indicated in (B)], respectively. Insets in (D) and (E) are the corresponding distribution of boundary spacing (left) and the SAED pattern (right). The sample coordinates in (D) and (E) are identical to that in (A). (F) A dark-field longitude-sectional TEM image corresponding to that in (E).

maximum intensity of ~ 6), which is consistent with the elongated SAED spots (Fig. 1E), indicates heavy shear deformation in the top

surface layer during SMGT processing and operative dislocation activities in the 2D NL structures (21).

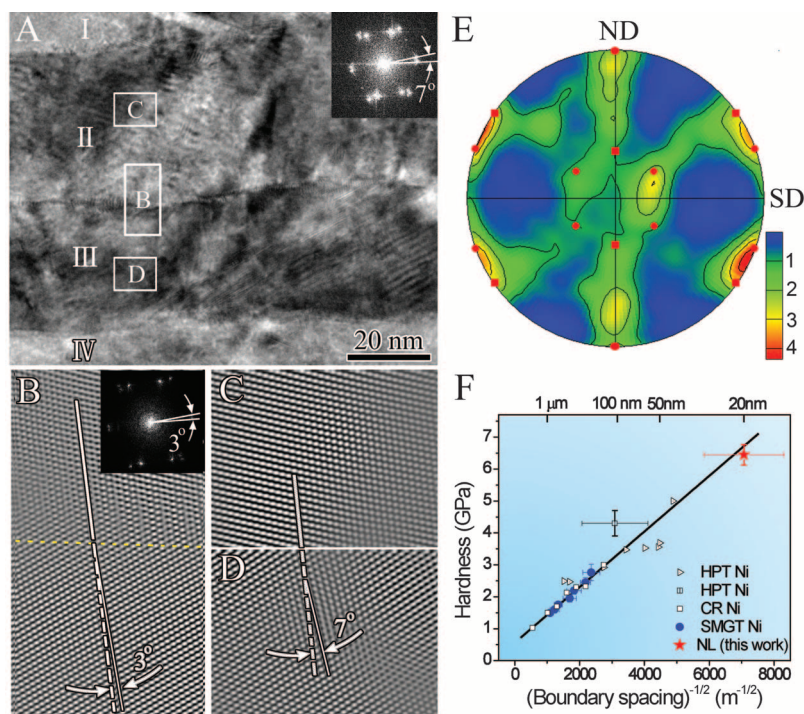


Fig. 2. Boundary structure, texture, and hardness of the NL structures. (A) A HRTEM image of the NL structures containing four lamellae (labeled as I, II, III, and IV). (Inset) A FFT image of lamellae II and III. (B) A Fourier-filtered image shows a contiguity of (11-1) atomic plane in lamella "II" to (111) in lamella "III," with a misorientation angle of 3° across the II/III boundary (yellow dashed line). (Inset) The FFT image also shows superimposition of two {111} planes, with a small misorientation angle. (C and D) Lattice images of lamella "II" and "III," showing that one of the closely packed {111} planes of II (2C) is inclined by 7° to III (2D). (E) {111} Pole figure of the NL structures after annealing at 540°C for 1 hour. The idea orientations of two main shear texture components are indicated with solid squares, $\{100\}\langle 011\rangle$; and solid circles, $\{111\}\langle 112\rangle$. (F) Hall-Petch plot for the UFG and NG structures in Ni samples processed via different techniques reported in the literature (10, 18, 22). The measured hardness of the NL structures (red star) is included for comparison by taking the lamellar thickness equivalent to grain size.

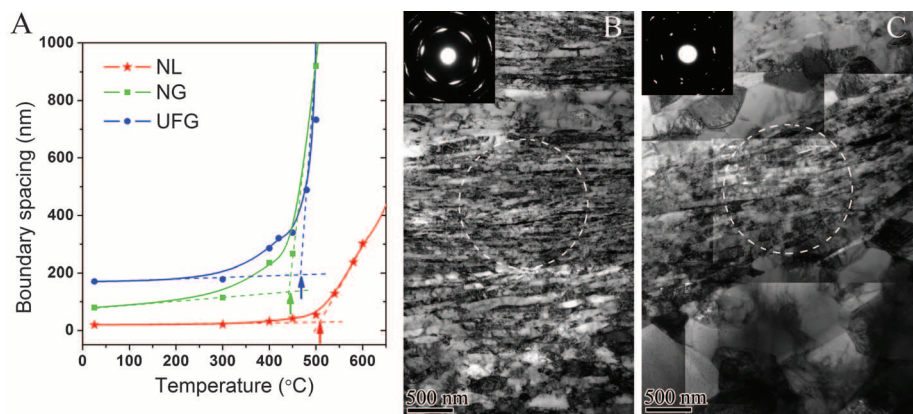


Fig. 3. Thermal stability of the NL structure. (A) Variations of boundary spacing of the UFG, NG, and NL structures as a function of annealing temperature (for 1 hour). (B) A bright-field TEM image of the alternative NG/NL structures at a depth of $\sim 80\ \mu\text{m}$ in the SMGT Ni sample. (C) A bright-field TEM image of the alternative NG/NL structures in the SMGT Ni sample after annealing at 500°C for 1 hour. (Inset) SAED patterns obtained from the respective dashed-line circled regions.

Vickers hardness measurements in the cross-sectional samples indicated that in the UFG layer in a depth span of 80 to $\sim 600\ \mu\text{m}$, hardness varies from 2.76 ± 0.26 to 1.40 ± 0.05 GPa corresponding to different structural sizes. These results are consistent with the reported data for pure Ni (10, 18, 22) and the Hall-Petch relation (Fig. 2E). Measured hardness of the NL structures at 10 to $\sim 50\ \mu\text{m}$ deep averaged 6.4 ± 0.32 GPa. This value is much higher than that in Ni samples processed via plastic deformation reported in the literature (5, 10, 11, 18) and is comparable with that of the electrodeposited Ni with grain sizes of $<20\ \text{nm}$ (23). Taking lamellar thickness of the NL structures as the equivalent grain size, we found that its hardness lies on the extrapolated Hall-Petch line (Fig. 2E). Such an agreement suggests that the NL boundaries are as effective in resisting dislocation motion as the conventional high-angle GBs. In fact, previous studies showed that contribution of low-angle boundaries to strength is comparable with that of high-angle GBs in strain-induced NG metals (11, 24). In addition, presence of substructures inside lamellae [such as dislocations and twin boundaries as revealed in HRTEM observations (fig. S3)] may provide additional hardening.

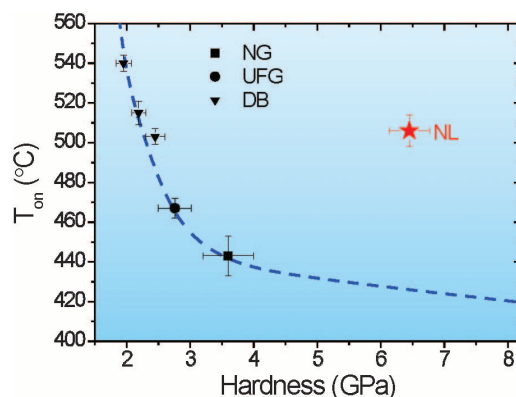
Dislocations are mainly presented at the low-angle boundaries in deformed metals, whereas the dislocation density within the volumes between the boundaries is one or two orders of magnitude lower and hence can be neglected (10, 11, 24). The dislocation density in low-angle boundaries (ρ_{LAB}) is calculated by $\rho_{\text{LAB}} = f_{\text{LAB}} S_v \rho_A$, where f_{LAB} is the fraction of low-angle boundaries, S_v is the boundary area per unit volume, and ρ_A is the dislocation density per unit area of boundary [for a mixed tilt and twist boundary $\rho_A = 1.5\theta/b$ (10, 24), θ is the average misorientation angle of low-angle boundaries and b is the Burgers vector]. With the measured parameters (table S1), a dislocation density of $\sim 1 \times 10^{15}\ \text{m}^{-2}$ was obtained for the UFG structures (120 μm deep from the surface), which is in accordance with the measured result ($\sim 2 \times 10^{15}\ \text{m}^{-2}$) in a torsion-deformed Ni at a comparable strain (25). For the NL structures (40 μm deep from the surface), dislocation density is $\sim 2.4 \times 10^{16}\ \text{m}^{-2}$, which is 20 times greater than that in the UFG. With this dislocation density, hardness of the NL structures can be calculated in terms of the Taylor hardening mechanism by taking it as 3 times the yield stress (10, 24)

$$H_v = 3(\sigma_0 + M\alpha Gb\sqrt{\rho_{\text{LAB}}}) \quad (1)$$

where σ_0 the frictional stress, M is the Taylor factor, α is a constant, and G is the shear modulus. The calculated hardness is 6.7 GPa, which is very close to the measured result (6.4 GPa), verifying the estimated dislocation density.

Thermal stabilities of these microstructures were examined by measuring boundary spacing under TEM after isothermal annealing at 300°C to

Fig. 4. Correlation of thermal stability and hardness. The onset temperature (T_{on}) versus hardness for various microstructures [UFG, NG, and dislocation boundaries (DBs)] in the SMGT Ni at different depths. Solid triangles denote DBs at depths of ~150, 200, and 300 μm from the treated surface.



900°C for 1 hour: 3D UFG structures at ~100 μm deep, 3D NG structures (average size of ~70 nm) at 60 to ~70 μm deep, and 2D NL structures. As in Fig. 3A, no obvious increment in the boundary spacing was detected for these structures after annealing below 300°C. The onset temperature for obvious grain coarsening (T_{on}) is ~443°C for the NG structures and is slightly higher for the UFG (467°C). This is in accordance with the general trend that coarsening temperature decreases for smaller grains (26). For the NL structures, it is surprising to see a much higher onset temperature for lamella thickening of ~506°C. This instability temperature is in agreement with that for the dislocation boundaries in deep layers of the sample (varying from 500° to 540°C, depending on the boundary spacing). The comparable T_{on} of the dislocation boundaries and the NL boundaries implies their similarities in structure.

To verify this observation, the as-SMGT sample was annealed at 500°C (for 1 hour), in between T_{on} of the 3D NG and the 2D NL structures, followed by TEM observations of the alternative NG/NL structures at a depth of ~80 μm . It is seen from Fig. 3, B and C, that the original NG structures transformed into micrometer-sized dislocation-free equiaxed grains—a typical recrystallization product—whereas the NL structures, apart from the slightly increased lamellar thickness due to a recovery process, retained their morphologies without obvious recrystallization. The 2D NL structures with a lamellar thickness of 20 nm are thermally more stable than are the 3D NG structures with grain sizes of 70 nm. The combination of greater hardness and thermal stability in the 2D NL structure is shown in Fig. 4.

No contamination was detected in the sub-surface layer deeper than 5 μm , under the resolution limits of an electron probe microanalyzer (15). The higher thermal stability of the 2D NL structures relative to the 3D UFG and NG structures may be attributed to the low excess energy and low mobility of the low-angle boundaries (27), as well as the extremely large radius of the 2D lamellae, which considerably reduces the capillary force for boundary migration. In addition, the orientation pinning due to the strong textured

lamellae (28), as well as the suppressed recrystallization nucleation kinetics by the laminated structure in extremely small dimensions (29), may also contribute to the elevated stability.

Formation of the NL structures is reasonably attributed to the large shear deformation with very high rates and large strain gradients in the top surface layer of the SMGT sample, which is distinct from the conventional heavy plastic deformation processes such as high-pressure torsion (HPT) and cold rolling. High strain rates promote dislocation multiplication relative to their annihilation (11, 30). The much larger strain gradients in the top surface layer of the SMGT sample than that in the HPT process (typically ~0.04 μm^{-1}) means a much higher geometrically necessary dislocation density is generated because it is proportional to the strain gradient (14). Formation of more low-angle boundaries in form of nanoscale laminated structures is energetically favorable, with an increased density of stored dislocations for minimizing the overall excess energy. Nanoscale laminated structures have also been observed in shear bands that are locally sheared at high rates with large strain gradients in UFG iron samples after compressive deformation (31) and in the nanotwinned Cu during dynamic compression (12). Most boundaries in the sheared regions (or shear bands) in the Cu are of low angle, with an average misorientation of ~7° (12). These observations, in accordance with our present study, suggest that formation of 2D NL structures with a very high dislocation density is a general scenario for strain-induced grain refinement in extremely small dimensions deformed at high strain rates with large strain gradients.

By generating such ultrahard and ultrastable NL structures in surface layers of engineering materials, enhancement in their wear resistance and fatigue properties is anticipated that are sensitive to the surface hardness and structure stability. The very high stored energy of the NL structure may elevate diffusion kinetics and chemical reactivity, facilitating surface modification of engineering alloys. With the simple and cost-effective processing technique, this nanostructure will find potential technological applications in a wide range of industrial manufacturing processes.

References and Notes

1. E. O. Hall, *Proc. Phys. Soc. B* **64**, 747–753 (1951).
2. N. J. Petch, *J. Iron Steel Inst.* **174**, 25–28 (1953).
3. G. I. Taylor, *Proc. R. Soc. London A Math. Phys. Sci.* **145**, 362–387 (1934).
4. R. Pippan, F. Wetscher, M. Hafok, A. Vorhauer, I. Sabirov, *Adv. Eng. Mater.* **8**, 1046–1056 (2006).
5. A. P. Zhilyaev *et al.*, *Acta Mater.* **51**, 753–765 (2003).
6. R. Pippan *et al.*, *Annu. Rev. Mater. Res.* **40**, 319–343 (2010).
7. T. H. Fang, W. L. Li, N. R. Tao, K. Lu, *Science* **331**, 1587–1590 (2011).
8. T. J. Rupert, D. S. Gianola, Y. Gan, K. J. Hemker, *Science* **326**, 1686–1690 (2009).
9. V. Y. Gertsman, R. Birringer, *Scr. Mater.* **30**, 577–581 (1994).
10. D. A. Hughes, N. Hansen, *Acta Mater.* **48**, 2985–3004 (2000).
11. Z. P. Luo, H. W. Zhang, N. Hansen, K. Lu, *Acta Mater.* **60**, 1322–1333 (2012).
12. F. Yan, H. W. Zhang, N. R. Tao, K. Lu, *J. Mater. Sci. Technol.* **27**, 673–679 (2011).
13. Y. S. Li, N. R. Tao, K. Lu, *Acta Mater.* **56**, 230–241 (2008).
14. M. F. Ashby, *Philos. Mag.* **21**, 399–424 (1970).
15. Materials and methods are available as supplementary materials on Science Online.
16. W. L. Li, N. R. Tao, K. Lu, *Scr. Mater.* **59**, 546–549 (2008).
17. J. Seviliano Gil, in *Evolution of Deformation Microstructures in 3D*, C. Gundlach *et al.*, Eds. (Denmark Risø National Laboratory, Denmark, 2004), pp. 1–11.
18. H. W. Zhang, X. Huang, N. Hansen, *Acta Mater.* **56**, 5451–5465 (2008).
19. H. Gleiter, *Acta Mater.* **48**, 1–29 (2000).
20. F. Montheillet, L. Cohen, J. J. Jonas, *Acta Metall.* **32**, 2077–2089 (1984).
21. B. Chen *et al.*, *Science* **338**, 1448–1451 (2012).
22. F. Dalla Torre, P. Spätig, R. Schaublin, M. Victoria, *Acta Mater.* **53**, 2337–2349 (2005).
23. F. Dalla Torre, H. Van Swyghoven, M. Victoria, *Acta Mater.* **50**, 3957–3970 (2002).
24. N. Kamikawa, X. Huang, N. Tsuji, N. Hansen, *Acta Mater.* **57**, 4198–4208 (2009).
25. E. Schaffer *et al.*, *Phys. Status Solidi A Appl. Res.* **175**, 501–511 (1999).
26. F. J. Humphreys, M. Hatherly, *Recrystallization and Related Annealing Phenomena* (Pergamon, Oxford, UK, 2004).
27. Y. Huang, F. J. Humphreys, *Acta Mater.* **48**, 2017–2030 (2000).
28. R. D. Doherty *et al.*, *Mater. Sci. Eng. A* **238**, 219–274 (1997).
29. M. Niewczas, O. Engler, J. D. Embury, *Acta Mater.* **52**, 539–552 (2004).
30. L. Farbaniec, A. Abdul-Latif, J. Gubicza, G. Dirras, *Adv. Eng. Mater.* **14**, 1027–1033 (2012).
31. Q. Wei, D. Jia, K. T. Ramesh, E. Ma, *Appl. Phys. Lett.* **81**, 1240–1242 (2002).

Acknowledgments: We thank X. Si for assistance in sample preparation and X. X. Huang for critical comments. We are grateful for financial support of the Ministry of Science and Technology of China (grant 2012CB932201), the National Natural Science Foundation (grants 51231006 and 51171182), and the Danish-Chinese Center for Nanometals (grants 51261130091 and DNR86–5).

Supplementary Materials

www.sciencemag.org/content/342/6156/337/suppl/DC1
Materials and Methods
Supplementary Text
Figs. S1 to S3
Tables S1 and S2
References (32)

1 July 2013; accepted 10 September 2013
10.1126/science.1242578